Characterization of InGaAs-based cameras for astronomical applications using a new VIS-NIR-SWIR detector test bench

Karsten Schindler[a,b,c], Jürgen Wolf[b,c] and Alfred Krabbe[c]

[a]Max-Planck-Institut für Sonnensystemforschung, Justus-von-Liebig-Weg 3, 37077 Göttingen, Germany

[b]SOFIA Science Center, NASA Ames Research Center, Mail Stop N211-1, Moffett Field, CA 94035, USA

[c]Deutsches SOFIA Institut, Universität Stuttgart, Pfaffenwaldring 29, 70569 Stuttgart, Germany

ABSTRACT

A new test bench for detector and camera characterization in the visible and near-infrared spectral range between 350 - 2500 nm has been setup at the Max Planck Institute for Solar System Research (MPS). The detector under study is illuminated by an integrating sphere that is fed by a Czerny-Turner monochromator with quasi-monochromatic light. A quartz tungsten halogen lamp is used as a light source for the monochromator. Si- and InGaAs-based photodiodes have been calibrated against secondary reference standards at PTB (Germany), NPL (UK) and NRC (Canada) for precise spectral flux measurements. The test bench allows measurements of fundamental detector properties such as linearity of response, conversion gain, full well capacity, quantum efficiency (QE), fixed pattern noise and pixel response non-uniformity.

The article will focus on the commissioning of the test bench and subsequent performance evaluation and characterization of a commercial camera system with a 640×480 InGaAs-detector, sensitive between 900 to 1650 nm. The study aimed at the potential use of InGaAs cameras in ground-based and airborne astronomical observations or as target acquisition and tracking cameras in the NIR supporting infrared observations at longer wavelengths, e.g. on SOFIA. An intended future application of the test bench in combination with an appropriate test dewar is the characterization of focal plane assemblies for imaging spectrometers on spacecraft missions, such as the VIS-SWIR channel of MAJIS, the Moons and Jupiter Imaging Spectrometer aboard JUICE (Jupiter Icy Moons Explorer).

Keywords: detector and camera characterization, test bench, InGaAs, infrared astronomy, photometry, near-infrared, telescope tracking, SOFIA

1. INTRODUCTION

The Max Planck Institute for Solar System Research (MPS) is participating in a variety of proposals for imaging infrared spectrometers on future spacecraft missions (e.g. MAJIS on JUICE[1], MARIS on MarcoPolo-R[2]) with the aim to provide the focal plane assembly (FPA) and detector electronics for read-out. Common to all proposals is the requirement to implement a FPA that is sensitive both to visible and infrared wavelengths (substrate-removed HgCdTe hybrid CMOS arrays). This allows a significant reduction is system complexity and therefore mass and power requirements of the instrument, as a separate channel with a Si-based detector can be avoided. This also evades intercalibration issues between different channels. To test and optimize the detector and front end electronics breadboard during development, to study degradation after radiation tests and to characterize flight hardware before integration into the instrument, a new test bench was necessary.

Aside of their use in spaceborne instruments, the same IR detector technology has a large number of applications on ground-based and airborne astronomical observatories. While HgCdTe arrays have become the standard choice thanks to their very high quality, their high cost often prohibits them to be used at smaller observatories or in instruments that need to follow a low cost approach. Another significant cost driver is the detector dewar that requires either a LN2 supply or

Further author information: (Send correspondence to K.S.)
K.S.: E-mail: kschindler@sofia.usra.edu, Telephone: +1 650 604 2555
J.W.: E-mail: jwolf@sofia.usra.edu
A.K.: E-mail: krabbe@dsi.uni-stuttgart.de

Ground-based and Airborne Telescopes V, edited by Larry M. Stepp, Roberto Gilmozzi, Helen J. Hall, Proc. of SPIE Vol. 9145, 91450X • © 2014 SPIE
CCC code: 0277-786X/14/$18 • doi: 10.1117/12.2057052

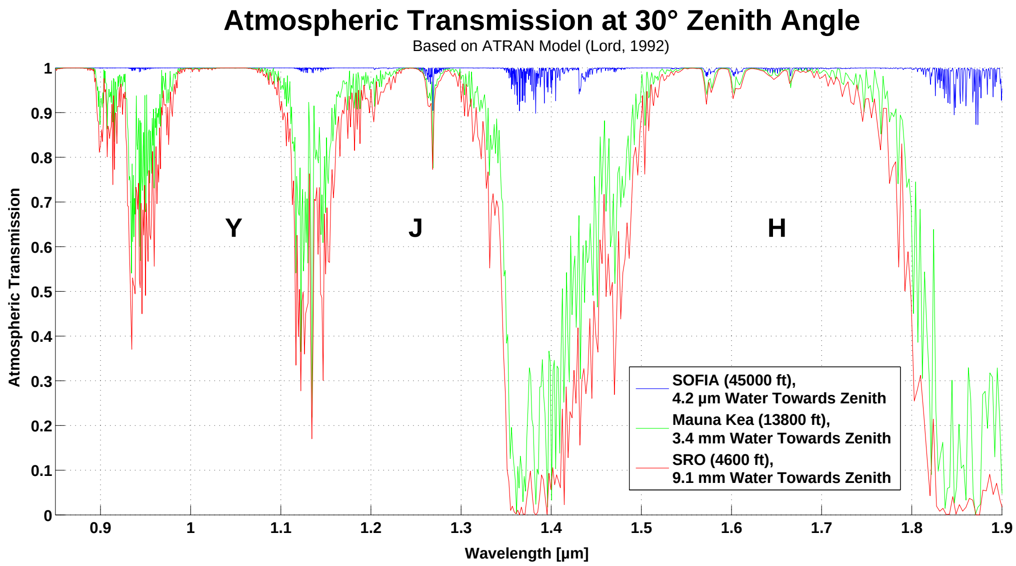

Figure 1: Atmospheric transmission at a Zenith angle of 30° in the wavelength range of InGaAs detectors, modeled with ATRAN (Lord et al, 1992[3]) at various elevations. The low-altitude site of the University of Stuttgart's 60 cm telescope (1405 m) has no significant disadvantage in the Y, J and H band compared to premium elevation sites such as Mauna Kea (4207 m). An application on SOFIA as a target acquisition, guiding and tracking camera would be practically under ideal conditions as less then 1% of water vapor overburden remains above flight altitude. This emphasizes the potential of InGaAs cameras for ground-based and airborne observations. (Data obtained from ATRAN webservice: https://atran.sofia.usra.edu)

a closed cycle, Stirling or pulse tube cooler, which can also introduce unwanted vibrations in the system. Especially for small, sub-meter to one-meter class telescopes, dewar-cooled IR arrays usually exceed budgets and operational possibilities, especially if these systems shall work completely unattended and autonomous at a remote site without personal. The same applies to cameras on balloons or airplanes where the most cost-effective approach would be a self-contained system which utilizes just a multi-stage Peltier cooler.

The 0.9 - 1.65 µm wavelength range of standard InGaAs fully covers the common Y and J bandpasses and some part of the H band. The bandgap energy of standard InGaAs still allows thermoelectrical cooling to reach acceptable dark current levels. Moreover, thermal background of the telescope and camera housing is not yet an issue considering the cut-off wavelength of InGaAs, so cooled optics are not required in front of the detector. This simplifies the camera design to a great extent, and compact camera packages that are similar to commercial high-end Peltier-cooled CCD cameras are possible. These advantages and the resulting cost reduction put the inability to cover the K band into perspective. A number of new Peltier-cooled NIR cameras with InGaAs arrays have recently entered the market, and the question evolved which quality and precision they can achieve.

A prime application would be the new 60 cm telescope of the University of Stuttgart at Sierra Remote Observatories (SRO) near Auberry, California. As illustrated in Figure 1, the moderate elevation of SRO (1405 m) provides no significant degradation in atmospheric transmission in the JHK bandpasses. Milone and Young[4] discussed how smaller telescopes at lower elevations are still able to provide high precision photometry in the NIR and noted that typical filter bandpasses in IR-astronomy have been developed according to the needs of high elevation sites, not for general purpose use. With a minimal modification in filter bandpass, sub-meter size telescopes could provide a significant contribution in the NIR especially for time-domain studies thanks to their high availability and low cost.

We see good scientific potential in the use of InGaAs detectors for photometric measurements: Most of the spectral energy of M-type dwarfs, the most common stellar type in our galaxy, just falls into the spectral range of InGaAs. This makes these detectors especially interesting for exoplanet transit surveys and follow-up observations around M-type dwarfs, where transiting planets are much easier to detect due to their much shorter periods and larger relative magnitude drop. Other fields of interest are supernova follow-up observations and studies of variable stars.

A second long-term interest in InGaAs camera systems would be their application for target acquisition, guiding and tracking on SOFIA. Currently, three Si-based CCD cameras are used for this purpose, allowing telescope tracking on stars down to V = 16 mag with the recently upgraded focal plane imager (FPI+)[5]. Although this limiting magnitude allows observations almost in the entire sky considering the availability of guide stars, certain areas that are of high interest for IR astronomy such as star formation regions in dark clouds (f.e. IRAS 16293-2422A) do not have a guide star with sufficient V magnitude within the 8 arcmin field of view of the FPI+. This makes it necessary to guide with the fine field imager (FFI) that provides a much larger field (67 arcmin), but consequently a much smaller resolution. The availability of sufficiently bright stars is much more relaxed at longer wavelengths as can be seen from the 2MASS catalog. Besides the large abundance of M-type stars, interstellar extinction is greatly reduced with increasing wavelength. Telluric absorption bands play an insignificant role on an airborne observatory (c.f. Figure 1), so there are practically no transmission losses between 0.9 - 1.65 μm which enables maximum sensitivity. These factors lead to a high availability of stars that are sufficiently bright for telescope tracking in the spectral range of InGaAs detectors.

In this paper, we present first test results of a Princeton Instruments NIRvana: 640 camera which utilizes a thermo-electrically cooled Xenics-built InGaAs array. This camera was one of two models that were tested with the new test bench in early 2013. A study with similar goals was published by Sullivan et al.[6] in 2013 who characterized a FLIR APS640C InGaAs detector (640×512, 25 μm pitch) with custom-built electronics. On-sky tests of a Xenics Xeva-1.7-640 (640×512, 20 μm pitch) camera have been conducted by Kohl[7] in 2013. A recent review by Hodapp[8] summarizes the potential of NIR imaging on sub-meter class telescopes. These recent activities emphasize the rising interest of the astronomical community in this detector technology, and we hope to contribute more insights into currently available camera systems with this paper.

2. TEST BENCH SETUP

2.1 Concept

The aim of the test bench is to irradiate the detector under test uniformly and stably with a light flux of known intensity, wavelength and bandpass in a spectral range from 350 - 2500 nm. Two approaches have been considered: 1) To use a source with a known flux, to measure the transmission of each optical element in the illumination system and to calculate the irradiance at the detector. 2) To treat the source and the illumination system as a "black box" and to use calibrated reference detectors to measure the irradiance in the detector plane.

A blackbody radiator with narrow-band filters would have provided a flux that can be calculated with high accuracy, but due to the requirement that the test bench needs to cover visible and NIR/SWIR wavelengths simultaneously, it was not an option. Apart of this, a large number of filters would have been necessary to cover the large spectral range with satisfying resolution for quantum efficiency measurements. A monochromator with a quartz tungsten halogen (QTH) lamp was chosen instead as a continuously tunable light source. QTH lamps emit a flux that is hardly analytically predictable as it varies greatly from lamp to lamp, degrades and slightly alters spectrally over time. It is also sensitive to the thermal environment in the lamp housing and quartz glass bulb. The use of calibrated halogen lamps was discarded as impractical and not economical. Moreover, the reflectivity of the gratings in the monochromator depend on incidence angle and polarization of the incoming radiation. Datasheets of gratings only provide reflectivity in Littrow configuration (diffraction angle = incidence angle), but the gratings in the monochromator turret are not operated in this condition. Polarization can be affected by filament structures in the lamp and stress induced birefringence in the quartz glass bulb. All these factors would lead to a large uncertainty of any analytical calculation of the irradiance at the detector plane. It was clear that only a reference detector based approach was feasible.

2.2 Illumination System

A simplified schematic view of the light path is illustrated in Figure 2. A Horiba iHR320 Czerny-Turner monochromator (f = 320 mm, f/4.1) is used to provide quasi-monochromatic light. A 250 W low-voltage QTH lamp driven by a 24 V / 10.4 A DC low-ripple power supply acts as a light source. The LSH-T250 lamp housing contains a rectangular 15.8 mm $\times$ 12.4 mm field stop located 16 mm in front of the lamp filament to reduce stray light. A concave mirror with a diameter of 57 mm and a focal ratio of f/4.5 focuses the light beam on the entrance slit of the monochromator. A fan at the bottom side of the lamp housing provides forced-air cooling. Table 1 provides an overview on the three gratings that are mounted in the grating turrett. Additionally, the monochromator offers a port for purging with dry air or nitrogen. Likewise to infrared astronomy, atmospheric water absorption becomes an issue for precise calibration work towards longer wavelengths. As an example, Figure 5 illustrates how varying humidity levels influence absorption around 1.4 μm (c.f. Figure 1).

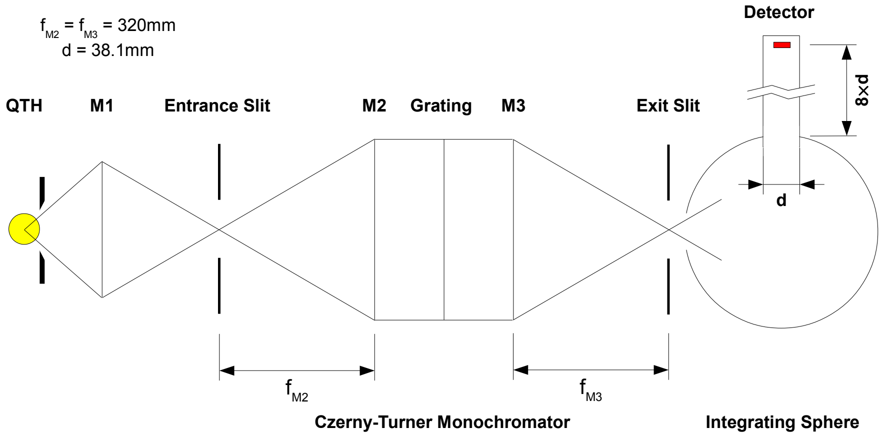

Figure 2: Schematic diagram of the test bench.

Table 1: Properties of the three plane gratings which are mounted in the grating turret of the Horiba iHR320 monochromator[9].

Grating No.	1	2	3
Horiba reference No.	530 24	510 15	510 21
Groove density [gr/mm]	1200	600	300
Blaze wavelength [nm]	500	1000	2000
Specified spectral range [nm]	360 - 1250	700 - 2000	1500 - 4000
Master grating for replica	Holographic	Mechanically ruled	Mechanically ruled
Size, blaze angle	68 mm × 68 mm × 9 mm[a], 17°27’		
Substrate material, coating	Pyrex blank with epoxy resin, aluminum coated		

[a] 2 - 4 mm border to grating edge without grooves.

Table 2: Longpass filters mounted in the internal filter wheel of the Horiba iHR320 monochromator.

Filter Wheel Position No.	2	3	4
Producer	Schott	Schott	NOC Ltd.
Type	Colloidally colored glass	Ionically colored glass	AR coated Germanium
Principle	Absorption	Absorption	Reflection
Designation	RG665	RG1000	7020005
Diameter [mm]	25	25	25
Thickness [mm]	2	2	3
50% cut-on wavelength [nm]	663	979	1810

To avoid changes in light flux due to changes in humidity during measurements, purging of the monochromator becomes necessary.

The monochromator has an internal filter wheel mounted behind the entrance slit. It contains three longpass filters of 1 inch diameter which are used to suppress higher orders of diffracted light. Table 2 gives a summary on their properties. Entrance and exit slits are motor-driven and adjustable in width from 0 - 7 mm in 6.25 µm intervals. Slit height can be manually adjusted to 1 mm or 15 mm. The exit slit of the monochromator is coupled to a 6 inch PTFE integrating sphere (Newport Model 70675) with 1.5 inch exit ports.

2.3 Reference Detectors

As all measurements depend entirely on the stability of the emitted spectral flux of the QTH lamp, irradiance has to be measured in the detector plane before and after each characterization measurement to make sure that conditions have been constant. The test bench will later be positioned in front of the MgF_2 window of a LN2-cooled detector dewar. As the photodiodes need to be placed at the detector plane, the housings had to be manufactured for vacuum conditions in terms of vacuum compatible, outgassing free PCBs, cables and black paint and good thermal conductivity. While camera and reference detectors have been manually exchanged for the camera characterization presented in this paper, a linear stage will later allow a remotely controlled exchange with the FPA inside the dewar.

It turned out that the greatest challenge for the test bench was the availability of calibrated reference photodiodes beyond 1800 nm. Commercially calibrated devices do not exist in this spectral range. Reference detectors are calibrated underfilled, i.e. with a light spot that is smaller than the sensitive area of the detector. When used for irradiance measurements, this implies that the response across the sensitive area is uniform. While certain silicon diodes usually provide very good spatial uniformity[10,11], studies of InGaAs diodes are hard to find in literature. Within this work, it was not possible to study the spatial non-uniformity of a number of different InGaAs diodes from various manufacturers. We assume that non-uniformity does not exceed 2% on the purchased photodiodes, a number that appears conservative and reasonable based on data in the literature[12,13]. Another difficulty was that off-the-shelf InGaAs photodiodes with cut-off wavelengths beyond 1.65 µm and integrated Peltier-coolers were only available with diameters up to 3 mm. For irradiance measurements, the detector's aperture size needs to be precisely known. While this is relatively easy to achieve for large Si photodiodes by placing a very precisely manufactured aperture on top, it is challenging for photodiodes of just 3 mm diameter given their manufacturing and packaging tolerances within their TO-housings. Instead of severely limiting the size of the photosensitive area, it was decided to operate the InGaAs photodiodes overfilled (illuminated area exceeds annular anode), although this can lead to a super-linear response as shown by Corredera et al. (2003)[14]. However, for photocurrents on the order of 10^{-7} - 10^{-9} A as in our measurements, the linearity error is expected to be small[14].

In an attempt to control remaining measurement uncertainties, four different photodiodes with overlapping spectral response have been purchased from Hamamatsu and calibrated against secondary standards by various national laboratories: A large 10×10 mm^2 Si-diode of documented high quality with a precisely manufactured aperture with 8.5 mm diameter, a standard (lattice matched) InGaAs diode with 3 mm diameter, and two extended wavelength (lattice mismatched) InGaAs diodes with 3 mm diameter and different cut-off wavelengths. A second, identical 10×10 mm^2 Si-diode was purchased with a calibration provided directly by the manufacturer and used for system tests. Table 3 provides an overview of all reference detectors, which are pictured in Figure 3 in their vacuum-compatible housings. Their response curves are illustrated in Figure 4. The Peltier coolers in all InGaAs diodes were powered by a Hamamatsu C1103-04 temperature controller. During characterization measurements, the results from different photodiodes agreed within 2 - 2.5%.

Table 3: Available reference photodiodes that were calibrated against secondary standards at various national laboratories. All photodiodes have been manufactured by Hamamatsu and were operated unbiased.

No.	Material	Model	Size	Calibration Laboratory	Calibrated Range [nm]	Calibration Uncertainty
1	Si	S1337-1010BQ	10×10 mm^2	Hamamatsu	200 - 1180	not available
2	Si	S1337-1010BQ	10×10 mm^2	PTB, Germany	400 - 1100	≤ 0.3% (400-1000nm) ≤1.12% (1000-1100nm)
3	InGaAs	G8605-23	∅ 3 mm	NPL, UK	850 - 1650	≤ 0.82 % (≤1620nm)
4	InGaAs	G5851-23	∅ 3 mm	NRC, Canada	800 - 1950	1.06 ... 3.00%
5	InGaAs	G5853-23	∅ 3 mm	NRC, Canada	1100 - 2500	2.82 ... 4.97%

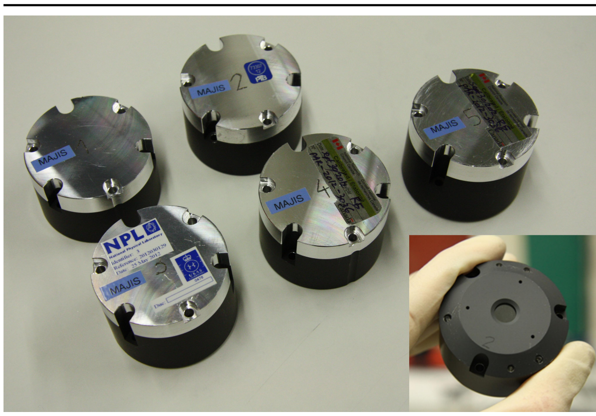

Figure 3: Reference photodiodes integrated in their vacuum compatible housings.

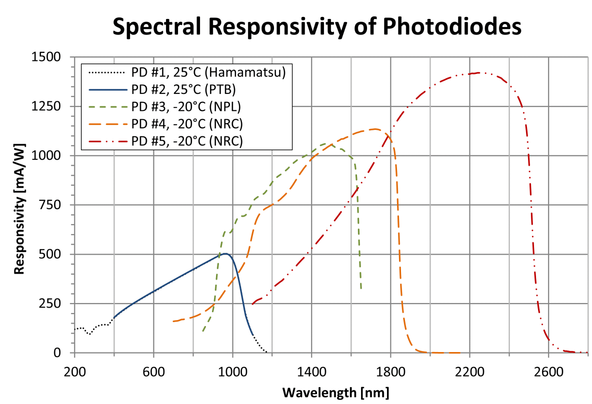

Figure 4: Calibrated spectral responsivity of all reference photodiodes.

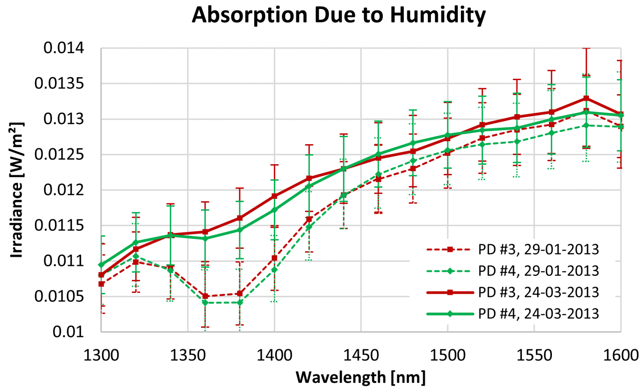

Figure 5: Exemplary irradiance measurements using two photodiodes on different days with different humidity in the lab. Water vapour absorption clearly affects irradiance when the monochromator is not purged.

A Keithley M6485 picoammeter was used to measure the short-circuit current of the photodiodes. Great care was exercised in proper shielding of all cables and grounding to reduce noise.

3. TESTED CAMERA

In this article, we focus on characterization results of a Peltier-cooled Princeton Instruments NIRvana: 640 InGaAs camera. Table 4 provides an overview of the camera's typical specifications; the package is illustrated in Figure 7. The camera was characterized at the slowest readout speed (2 MHz / 22 fps) to achieve lowest read noise. Being solely fan-cooled without circulating cooling liquid, the detector temperature could be stably locked at -90°C which left a margin of about 4 K to the lowest achievable temperature under full load of the Peltier element.

The InGaAs photodiode array is flip-chip bonded on top of a Si ROIC via indium solder bumps, forming a hybrid FPA of two different semiconductors. Details on the FPA architecture are not available, except that the FPA was manufactured by Xenics (S. Eck, Xenics USA, personal communication). Based on the camera's frame rate and two gain modes, it can be assumed that each pixel likely includes a charge transfer impedance amplifier (CTIA) which stores photoelectric charges in one of two selectable feedback capacitors: A large capacitor that allows imaging of a wide dynamic range (low gain) and a small capacitor providing high sensitivity (high gain) for high speed imaging with short exposure times. For some more information on Xenics' FPA design, see[17].

Table 4: Specifications of the NIRvana: 640 camera as provided by Princeton Instruments[15,16].

Sensor	Xenics-built FPA; 640 × 512 pixel, 20 μm pitch	
Cooling system	Multi-stage Peltier cooler	
Heat transfer	Forced air (fan), liquid coolant, or both	
Achievable sensor temperature	-80°C (air only), -85°C (air + 15°C liquid)	
Accuracy of temperature control	± 0.05°C	
Quantum efficiency	> 80% between 960 - 1600 nm	
Dark current (e^-/s)	≈ 300 e^-/s at -80°C, measured with a cold target at -174°C in front of camera	
Frame rate (readout speed)	22 (2 MHz), 55 (5 MHz), 110 (10 MHz)	
Interface	Gigabit Ethernet (GigE), up to 50 m cable length	
ADC resolution	16 bit	
Outer dimensions	194 × 173 × 148 mm^3 (including connectors)	
Weight	4.3 kg	
	High gain	Low gain
Full well capacity (e^-)	≥ 40,000	≥ 600,000
Typical system read noise (e^-)	< 120 e^-	n/a
Nominal conversion gain (e^-/DN)	1	14
Response non-linearity	< 2 % at exposure times > 20 ms	n/a

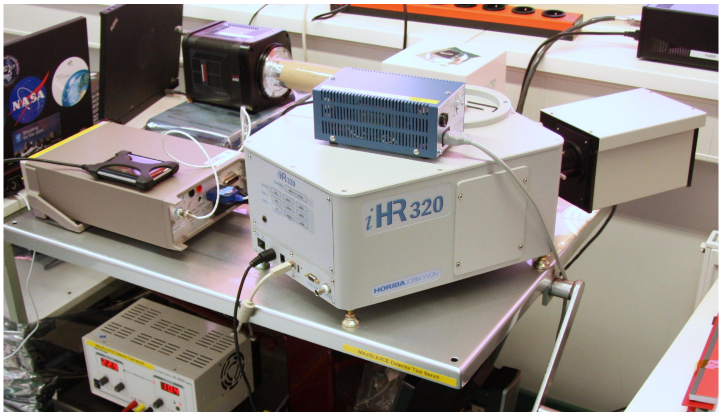

Figure 6: Lab setup during characterization measurements.

Figure 7: The Nirvana: 640 camera package.

4. MEASUREMENTS

The camera sensor was positioned behind the integrating sphere at a distance of eight exit port diameters to ensure sufficiently homogeneous illumination. The entrance and exit slit width were set to 4 mm, which lead to an effective bandpass of about 10 nm, varying slightly with grating and wavelength as listed in Table 5. Distance and bandpass are also in accordance with the recommendations in EMVA Standard 1288[18].

Camera cooling was started at least 1 h before the measurements to ensure the cooling system had reached a steady state and the camera was in thermal equilibrium. The illumination source was switched on 30 min before to ensure a constant illumination level and stable thermal environment. Constant irradiance was confirmed with the calibrated photodiodes before and after each imaging series. All image analysis has been done in Matlab.

4.1 Conversion gain and non-linear behavior

While lamp intensity was fixed, exposure time was altered incrementally (low gain: 200 µs steps / high gain: 20 µs steps) from the shortest integration time that the camera supported (1 µs) until saturation was clearly visible from the histogram of pixel values. At each exposure time, N=101 consecutive images were taken to have a sufficiently large sample size for variance (noise) calculations. The first image of each image sequence was discarded as it contained a systematic offset in DN, probably due to transient effects as electronics and clocking need to stabilize (e.g. thermal effects). The measurement was repeated at 950 nm, 1250 nm and 1550 nm to provide redundancy. Afterwards, the lens cap was placed on the camera and covered with aluminum tape to securely avoid any stray light on the detector that could result from increasing transparency of the plastic lens cap material at infrared wavelengths. 101 consecutive dark frames (the first being discarded) were taken at every exposure time that was previously used, whereas the shortest integration time of 1 µs represents the bias frame. A master dark frame was built for each exposure time step by calculating the median of all dark frames in the sequence. These master darks were subsequently used for offset correction.

CMOS detectors and IR hybrid FPAs usually inhibit a non-linear response to incoming radiation. Unlike CCDs, each pixel in a CMOS has to be seen as an individual detector as it consists of a photodiode and a number of transistors to reset the pixel, to buffer, amplify or read out charge. According to Janesick[19], non-linear response in CMOS detectors has its

Table 5: Grating - filter combinations used for QE measurements and resulting bandpass with a 4 mm entrance slit width.

Spectral Range [nm]	Grating	Filter	Bandpass with 4 mm Entrance Slit [nm]
400 - 700	1	-	10.39 - 10.06
700 - 800	1	2	10.06 - 9.85
800 - 1200	2	2	10.39 - 10.21
1200 - 1300	2	3	10.21 - 10.14
1300 - 1950	3	3	10.41 - 10.34
1950 - 2600	4	4	10.34 - 10.14

origin primarily in non-linearities in gain (V/V) and sensitivity (V/e$^-$). The first results from a non-linear amplification somewhere in the signal chain, while the second is due to a changing sens node capacitance as the amount of accumulated charge increases. Further sources of non-linearity can be the analog-to-digital converters and residual charge left behind in pixels after read-out, an effect known as image lag.

This is in particular problematic in the attempt to quantify the sensor's conversion gain. An erroneous estimate subsequently leads to deviations of other sensor parameters such as full well capacity, QE and read-noise. Bohndiek et al. (2008)[20] provide an overview on various methods for estimating conversion gain of CMOS detectors. Standard methods applied to CCD sensors such as mean-variance analysis or classic photon-transfer can not be applied anymore, as they assume linear response with illumination, small variance in conversion gain and uncorrelated noise sources. These assumptions do not hold for CMOS sensors. Instead, the non-linear compensation (NLC) method[19] or the non-linear estimation (NLE) method[21] have to be used to estimate conversion gain. While NLC provides a valuable way to diagnose and distinguish non-linearities (V/V or V/e$^-$) by decomposing the conversion gain into signal gain and noise gain, NLE allows a reliable estimation of QE[20].

A cosmetically clean, central area of the image of 80×60 pixels was analyzed. Figure 8 and 9 illustrate the decomposed shot noise and fixed pattern noise (FPN) components of the measurement at 1250 nm. A large non-linearity in response was observed at exposure times below ≈ 10 ms as can be seen in Figure 10. This is in accordance to the datasheet stating that non-linearity is only $< 2\%$ at exposure times > 20 ms (c.f. Table 4). The reason of this non-linear response could not be determined yet. The shot noise curve follows the expected slope of 0.5 only in a brief interval of about S = 14,000 - 20,000 DN. Likewise, the FPN curve has an expected slope of 1 only in the interval of S = 5,000 - 13,000 DN. The deviation

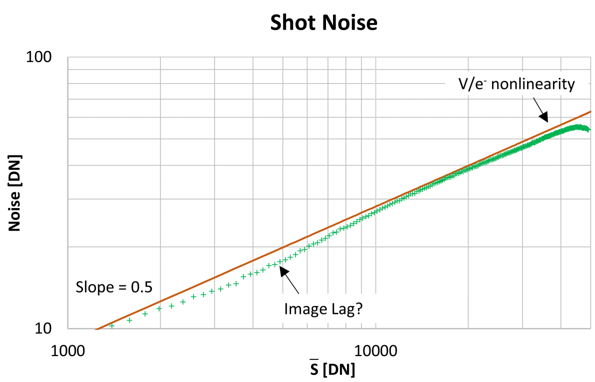

Figure 8: Decomposed shot noise component, showing a deviation from the expected slope of 0.5 in logarithmic scale at low and high signal levels.

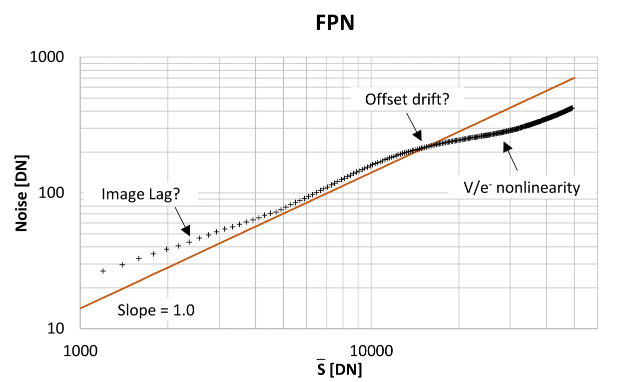

Figure 9: Decomposed fixed pattern noise component, not following a slope of 1 in logarithmic scale.

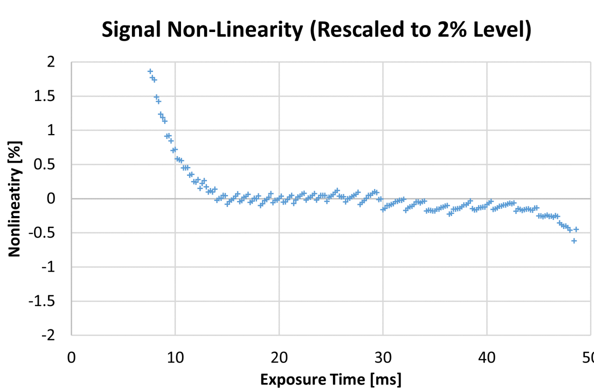

Figure 10: Residual from a linear fit of average signal vs. exposure time between S = 14,000 - 18,000 DN, the range in which shot noise follows a slope of 0.5 and linearity of the detector is most likely.

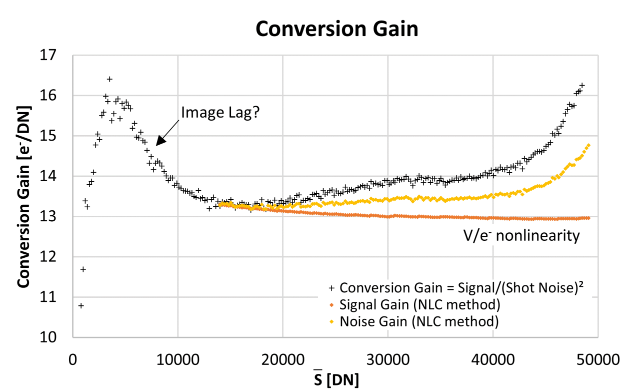

Figure 11: Conversion gain estimated by the standard approach for linear detectors (black) and decomposed signal and noise gain resulting from the NLC method.

in slope at high signal levels for both noise components indicates the presence of V/e$^-$ non-linearity - a change in sensitivity due to changing sense node capacitance with accumulated charge. The deviation of the shot noise curve at low signal levels could be indicative of image lag. However, the sudden change in slope of the FPN curve at about S = 15,000 DN might be due to an incorrect offset subtraction. As this effect can be seen in the PTC in all three measurements that were taken, it would imply a drift in offset during the dark frame acquisition, leading to erroneous or incomplete offset subtraction, or some systematic, not yet understood effect at higher signal levels. Further investigation of this behavior is necessary.

As the shot noise curve has a slope lower than 0.5 at signal levels below S ≈ 14,000 DN, a conversion gain estimate following

$$K = \frac{\bar{S}}{\sigma^2_{Shot}} \tag{1}$$

is severely in error in this range as can be seen from the black curve in Figure 11. An initial decrease in conversion gain with signal can be a hint for image lag[19].

The presence of erroneous conversion gain values at low signal levels is problematic for the application of the NLC method. This method assumes that conversion gain, signal gain and noise gain are equal at low signal levels provided that non-linearity is insignificant there, extrapolates higher signal level values from the initial low signal level based on accurate knowledge of exposure time and the irradiance of the detector, and subsequently calculates signal gain and noise gain from the extrapolated signal level and measured signal level in DN. In the present case, NLC was applied with the assumption that the detector responds linear between S = 14,000 - 18,000 DN. The resulting decomposition of signal and noise gain from the NLC method is illustrated in Figure 11 as well. The resulting signal gain is on the order of 13 - 13.3 e$^-$/DN.

Providing a different approach to the problem of conversion gain estimation, the NLE method[21] which calculates conversion gain as a function depending on signal was applied to the dataset. The result is illustrated in Figure 12. As can be seen, the conversion gain varies from K = 14 to 15.5 e$^-$/DN between S = 10,000 - 50,000 DN. This result is significantly larger compared to the NLC method, consequently leading to larger QE values in the next section, but also larger estimates of read noise. For the low gain mode, a system read noise of about 338 e$^-$ (K = 14) was found.

4.2 Quantum Efficiency

Measurements were prepared with ample camera cooling and illumination source uptime as described for the conversion gain measurements. After selecting an exposure time that resulted in a signal of about 65% of the datasheet's full well capacity at wavelengths around the expected peak sensitivity (≈ 1500 nm) of the camera, image sequences of N=101 consecutive images were taken with constant exposure time in 20 nm steps between 740 - 1740 nm using the grating and second order filter combinations given earlier in Table 5. Again, the first image of each sequence was discarded due to a systematic offset. Subsequently, N=101 consecutive dark frames were taken and median-combined to a master dark frame for offset subtraction. Before and after the measurements, spectral irradiance was measured in the same 20 nm intervals between 740 - 1740 nm using the calibrated photodiodes.

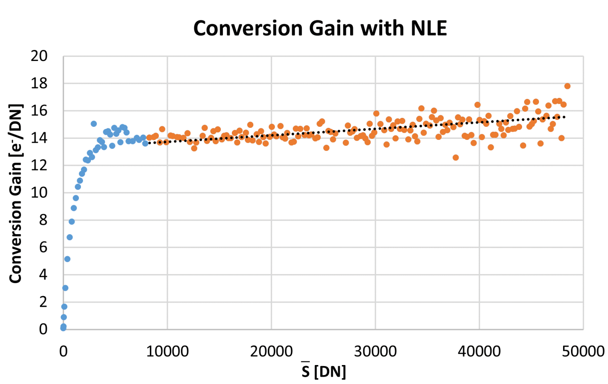

Figure 12: Conversion gain as a function of signal as estimated by the NLE method, varying from K = 14 - 15.5 e$^-$/DN (orange colored values).

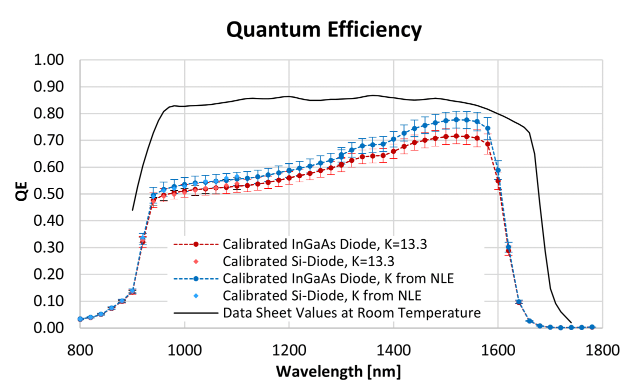

Figure 13: Quantum efficiency estimates based on a) the conversion gain from the NLC method and b) the signal-dependent conversion gain of the NLE method.

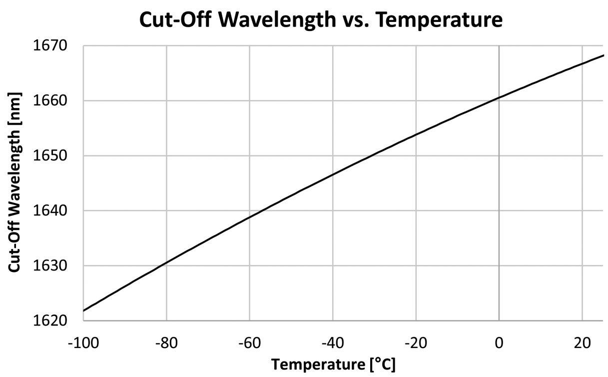

Figure 14: Cut-off wavelength as a function of temperature for $In_{0.53}Ga_{0.47}As$.

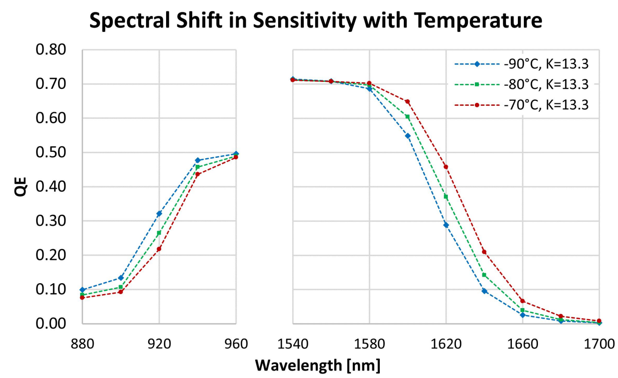

Figure 15: As bandgap energy decreases with temperature, the spectral sensitivity of the detector is blue-shifted. The shift in cut-on and cut-off wavelength was clearly seen between the measurements with a sensor temperature of -90°C, -80°C and -70°C.

The classic QE transfer method was applied[19]. Aside of the calibration uncertainty of the photodiodes (c.f. Table 3), the measurement uncertainty resulting from the setup (positioning uncertainty, possible but unknown non-uniformity and non-linearity of the photodiodes) was estimated as 3%. The resulting quantum efficiency values for the camera's InGaAs array are illustrated together with the estimated total errors in Figure 13, both for applying the conversion gain obtained from the NLC method and the signal-dependent conversion gain of the NLE method.

As the NLE conversion gain estimates are more representative for the detector array, the respective QE values appear more robust (c.f. blue curve in Figure 13). Still, the measured QE values are significantly lower than the values provided in the datasheet of the camera[15]. Note that the datasheet provides typical, not guaranteed QE values, though.

According to Pearsall[22], the band gap energy of standard $In_{0.53}Ga_{0.47}As$ is described by

$$E_g(T) = 0.812 - 3.26 \times 10^{-4} T + 3.31 \times 10^{-7} T^2 \text{eV} \tag{2}$$

which directly leads to the cut-off wavelength for each temperature as illustrated in Figure 14. For redundancy and to directly measure the spectral shift in sensitivity with decreasing temperature, QE measurements were repeated with a sensor temperature of -70°C, -80°C and -90°C. Figure 15 illustrates the blue shift of the cut-on and cut-off wavelength with decreasing temperature as a direct result from measurements.

4.3 Dark Current

A surprising behavior was found by evaluating dark frames with longer integration times. Figure 16 plots dark current in high gain mode as a function of integration time. While dark current was $\approx$ 458 e^-/s at a detector temperature of -70°C and decreased as expected to $\approx$ 385 e^-/s at -80°C, it increased dramatically to $\approx$ 1222 e^-/s at -90°C. Although cooling was stable at this temperature and left a margin of $\approx$ 4 K for the thermoelectrical cooler to avoid running it at full load, images degraded significantly as illustrated in Figure 17. It is still unclear what causes this effect. The sensor temperature of -90°C seems to be correct, as we would have otherwise not observed the same spectral shift in cut-on and cut-off wavelength from -80°C to -90°C as from -70°C to -80°C in the QE measurements (c.f. Figure 15). Further investigations of this behavior are necessary.

4.4 Autocorrelation Analysis

Capacitive coupling of neighboring pixels also affects the conversion gain and consequently QE estimates as signal that should have been recorded in the central pixel appears in neighboring pixels. This influences variance estimates.

A cosmetically clean region in the image was used to conduct an autocorrelation analysis[23] on 99 image pairs of 100 consecutive images from the dataset for conversion gain estimation. The analysis was repeated at various exposure times. Figure 18 shows a plot of an exemplary result. It has been estimated that the variance and therefore conversion gain

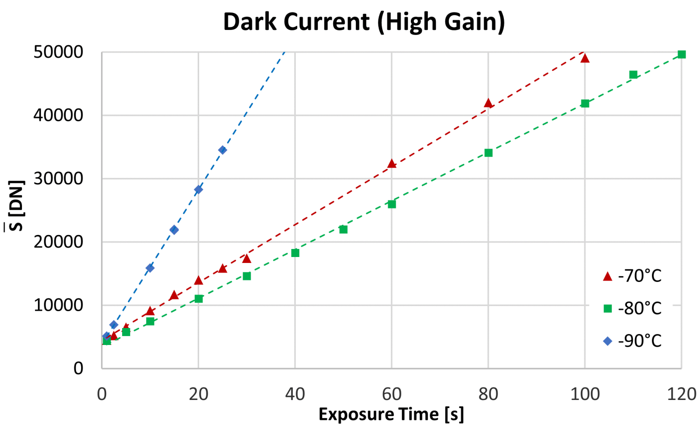

Figure 16: Dark current in high gain mode for various sensor temperatures. A significantly increased signal was observed at a detector temperature of -90°C.

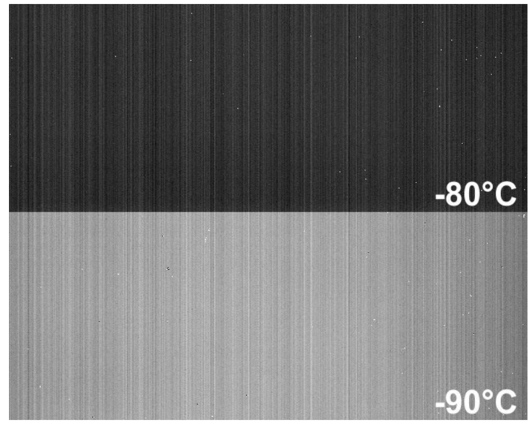

Figure 17: Degradation of dark frames (HG mode) between -80°C and -90°C. Both dark frames have an integration time of 20 s, show the same part of the detector and are equally scaled.

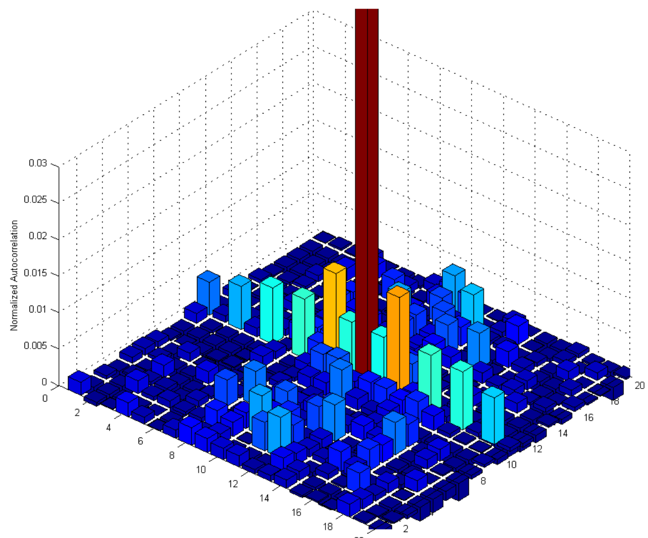

Figure 18: Result of an autocorrelation analysis of a cosmetically clean central 80×60 pixel region in the image.

is overestimated by 2% - a low value compared to other IR detectors in astronomy[24]. This corresponds to a capacitive crosstalk of a pixel of 0.25% to each of its four neighboring pixels. A regular pattern in column direction indicates correlation presumably caused by electrical crosstalk in the multiplexer during readout. Further investigations are necessary to clarify this effect.

5. ASTRONOMICAL APPLICATION

At the University of Stuttgart's 60 cm f/8 telescope, the camera would provide a field of view of 9.16×7.33 arcmin. The 20 µm pixel pitch translates to a plate scale of 0.86 arcsec/pixel. The Nyquist theorem establishes that critical sampling of a Gaussian PSF equals its standard deviation. This translates to an optimal plate scale where the FWHM of the PSF covers 2.36 pixels. However, the atmospheric seeing at visible wavelengths at the site of the telescope is typically around 1.5 arcsec FWHM, with good nights during summer reaching 1.0 arcsec. Therefore, we expect modest undersampling, also as atmospheric seeing should slightly improve towards the J / H band. Current InGaAs FPA developments[25] promise smaller pixel sizes in future cameras which would be beneficial for astronomical observations, but are not yet seen in commercial devices.

6. CONCLUSIONS AND FUTURE WORK

A Peltier-cooled, self-containing InGaAs camera would be a valuable instrument on a sub-meter to one-meter class telescope for photometric time-domain studies and on SOFIA to extend tracking capabilities. The presented camera could be a candidate for these applications, but further investigations are necessary to fully understand all effects that have been seen from measurements. Given that these effects are reproducible, corrections can be applied. A small data reduction pipeline can correct non-linearities in the acquired data to provide science-quality imaging data.

An extension of the test bench is planned. A chopper and lock-in amplifier have been purchased for future measurements at lower light levels (e.g. smaller bandpass) and will be commissioned soon. To operate bare IR focal plane assemblies with the setup, a dewar with a cold finger, heaters and a temperature controller for cool-down and temperature stabilization is necessary. A design to adapt the test bench to an existing system has been finalized and is pending to be implemented.

An on-sky test of the camera at the University of Stuttgart's 60 cm telescope and further lab tests are planned for winter 2014. Aside of some photometric measurements and a cross-check of quantum efficiency with stellar sources, we plan to study the temperature-dependent behavior of the camera in more detail and check for persistence effects after exposure of pixels to bright sources or saturation that could lead to leak current in subsequent images.

ACKNOWLEDGMENTS

K.S. especially thanks Andreas Nathues and Georg Tomasch at MPS for supporting this work and providing the necessary lab equipment and hardware that made these measurements possible. This work has been supported financially by a PhD fellowship of the *International Max Planck Research School on Physical Processes in the Solar System and Beyond*. K.S. also acknowledges financial support by the University of Stuttgart and the German Academic Exchange Service (DAAD) to continue parts of this research at NASA Ames Research Center in collaboration with the Deutsches SOFIA Institut (DSI).

Calibrations of the photodiodes have been conducted by Katrin Vogel and Dr. Lutz Werner (PTB Berlin, Germany), Rick Gerson (National Research Council, Canada) and Theo Theocharous and Subrina Harris (NPL, UK) who also provided valuable insights and discussions in the course of this work. Jürgen Schmidt's support at Innovent Jena was critical in obtaining an optimal black coating at NIR wavelengths. We would like to especially thank Norbert Gulde at Roper Scientific GmbH for providing a demo unit of the camera on short notice and free of charge for our lab investigations. The author also thanks Juanjo Piqueras for valuable discussions on CMOS detectors.

REFERENCES

[1] Langevin, Y., Piccioni, G., Eng, P., Filacchione, G., Poulet, F. and the MAJIS Team, "The MAJIS VIS-NIR Imaging Spectrometer for the JUICE Mission," *45th Lunar and Planetary Science Conference*, Abstract No. 2493 (March 2014).

[2] European Space Agency, "MarcoPolo-R Assessment Study Report," ESA/SRE(2013)4 (December 2013).

[3] Lord, S. D., "A New Software Tool for Computing Earth's Atmospheric Transmission of Near- and Far-Infrared Radiation," NASA Technical Memorandum 103957 (December 1992).

[4] Milone, E. F. and Young, A. T., "Infrared Passbands for Precise Photometry of Variable Stars by Amateur and Professional Astronomers," *Journal of the American Association of Variable Star Observers (JAAVSO)* **36**, pp. 110–126 (2008).

[5] Wolf, J., Wiedemann, M., Pfüller, E. and Lachenmann, M., "Upgrade of the SOFIA target acquisition and tracking cameras," *Proc. SPIE* **9145** (this conference), Paper No. 9145-31 (2014).

[6] Sullivan, P. W., Croll, B. and Simcoe, R. A., "Precision of a Low-Cost InGaAs Detector for Near Infrared Photometry," *Publications of the Astronomical Society of the Pacific* **125**, pp. 1021–1030 (2013).

[7] Kohl, S., "Application of an InGaAs NIR camera for photometry," *Contributions of the Astronomical Observatory Skalnat Pleso* **43**, pp. 246–247 (2014).

[8] Hodapp, K., "Infrared imaging and spectroscopy with small telescopes," *Contributions of the Astronomical Observatory Skalnat Pleso* **43**, pp. 200–208 (2014).
[9] HORIBA Jobin Yvon, "Scientific diffraction gratings / Custom gratings - Product catalog and capabilities," Rev. F (26 February 2009).
[10] Durak, M., Samadov, F. and Türkoglu, A. K., "Spatial Non-uniformity Measurements of Large Area Silicon Photodiodes," *Turkish Journal of Physics* **26**, pp. 375–380 (2002).
[11] Larason, T. C. and Bruce, S. S., "Spatial uniformity of responsivity for silicon, gallium nitride, germanium, and indium gallium arsenide photodiodes," *Metrologia* **35**(4), pp. 491–496 (1998).
[12] Durak, M., "Spatial non-uniformity analyses of radiometric detectors to identify suited transfer standards for optical radiometry," *The European Physical Journal - Applied Physics* **32**, pp. 193–197 (2005).
[13] Eppeldauer, G. P., Yoon, H. W., Zeng, J., Larason, T. C., Houston, J. M. and Khromchenko, V., "Extension of the NIST spectral power-responsivity calibration service to 2500 nm," *Metrologia* **49**(2), pp. S112–S117 (2012).
[14] Corredera, P., Hernanz, M. L., Gonzlez-Herrez, M. and Campos, J., "Anomalous non-linear behaviour of InGaAs photodiodes with overfilled illumination," *Metrologia* **40**(1), pp. S150–S153 (2003).
[15] Princeton Instruments, "NIRvana: 640 Datasheet," Rev. N1.2 (13 March 2013).
[16] Princeton Instruments, "NIRvana Camera System Manual," Version 3 (1 November 2013).
[17] Neys, J., Bentell, J., O'Grady, M., Vermeiren, J., Colin, T., Hooylaerts, P. and Grietens, B., "Cheetah: A high frame rate, high resolution SWIR image camera," *Proc. SPIE* **7106**, pp. 71061M–71061M–7 (2008).
[18] European Machine Vision Association, "EMVA Standard 1288 - Standard for Characterization of Image Sensors and Cameras," Release 3.0 (29 November 2010).
[19] Janesick, J. R., [Photon Transfer], *SPIE Press Monograph* **PM170**, SPIE Publications (2007).
[20] Bohndiek, S. E., Blue, A., Clark, A., Prydderch, M., Turchetta, R., Royle, G., and Speller, R., "Comparison of Methods for Estimating the Conversion Gain of CMOS Active Pixel Sensors," *IEEE Sensors Journal* **8**, pp. 1734–1744 (2008).
[21] Pain, B. and Hancock, B. R., "Accurate estimation of conversion gain and quantum efficiency in CMOS imagers," *Proc. SPIE* **5017**, pp. 94–103 (2003).
[22] Pearsall, T., "$Ga_{0.47}In_{0.53}As$ - A ternary semiconductor for photodetector applications," *IEEE Journal of Quantum Electronics* **16**, pp. 709–720 (1980).
[23] Moore, A. C., Ninkov, Z. and Forrest, W. J., "Quantum efficiency overestimation and deterministic cross-talk resulting from interpixel capacitance," *Optical Engineering* **45**(7), pp. 076402–076402–9 (2006).
[24] Finger, G., Dorn, R., Meyer, M., Mehrgan, L., Moorwood, A. F. M. and Stegmeier, J., "Interpixel capacitance in large format CMOS hybrid arrays," *Proc. SPIE* **6276**, pp. 62760F–62760F–13 (2006).
[25] Vereecken, W., Van Bogget, U., Colin, T., Vinelli, R.-M., Das, J., Merken, P. and Vermeiren, J., "A low-noise, extended dynamic range 1.3 megapixel InGaAs array," *Proc. SPIE* **8704**, pp. 870404–870404–8 (2013).